JOURNAL OF AIRCRAFT
Vol. 53, No. 4, July-August 2016

Modeling of Highly Flexible Multifunctional Wings for Energy Harvesting

Natsuki Tsushima* and Weihua Su†
University of Alabama, Tuscaloosa, Alabama, 35487-0280

DOI: 10.2514/1.C033496

In this paper, modeling of energy harvesting from transient vibrations of slender wings using piezoelectric transduction is implemented in a strain-based geometrically nonlinear beam formulation. The resulting structural dynamic equations for multifunctional beams are then coupled with a finite-state unsteady aerodynamic formulation, allowing for both energy harvesting and piezoelectric actuation with the nonlinear aeroelastic system. With the development, it is possible to provide an accurate, integral aeroelastic and electromechanical solution of both energy harvesting from and active control for wing vibrations, considering the geometrical nonlinear effects of slender wings. The current paper focuses on modeling the energy harvesting subsystem and exploring its impact on the multifunctional system. Vibrations of a slender multifunctional wing excited by both aeroelastic instability and external wind gusts will be considered as the sources of energy harvesting. All simulations will be completed in the time domain to accurately capture the nonlinear behaviors of the slender multifunctional wing. Based on the time-domain analysis, results of this effort illustrate that the piezoelectric energy harvesting from transient vibrations may provide adequate energy to support onboard sensor operations. In addition, results indicate that a well-tuned piezoelectric energy harvesting system may control the wing vibration using the shunt damping effect.

Nomenclature

A	=	cross-section area of the piezoelectric layer, m^2
a_0	=	local aerodynamic frame, with a_{0x} axis pointing to wing tip and a_{0y} axis aligned with zero lift line of airfoil
a_1	=	local aerodynamic frame, with a_{1y} axis aligned with airfoil motion velocity
B	=	body reference frame
$\bar{\mathbf{B}}$	=	electric displacement, C/m^2
$\mathbf{B}^F$, $\mathbf{B}^M$	=	influence matrices for the distributed forces and moments
$\mathbf{B}_v$	=	piezoelectric coupling matrix
B_v^{cs}	=	cross-sectional piezoelectric coupling matrix
b_c	=	semichord of airfoil, m
b_p	=	chordwise width of the piezoelectric layer, m
C_p	=	capacitance of the energy harvesting system, F
$\mathbf{D}$	=	piezoelectric material stiffness matrix
d	=	distance of midchord in front of beam reference axis, m
$\mathbf{E}$	=	electric field, V/m
$\mathbf{e}$	=	piezoelectric coupling, C/m^2
e_{31}	=	transverse piezoelectric coupling, C/m^2
$\mathbf{F}^{\text{dist}}$, $\mathbf{F}^{\text{pt}}$	=	distributed and point forces
$\mathbf{F}_i$	=	influence matrices in inflow equations with independent variables in which i is equal to 1, 2, and 3)
$\mathbf{g}$	=	gravity acceleration column vector, m/s^2
H	=	altitude, m
H_w	=	transfer function
$\mathbf{h}$	=	absolute positions and orientations of beam nodes
i	=	electric current in a circuit of energy harvesting system, A
$\mathbf{J}$	=	Jacobian matrix
L_w	=	scale of turbulence, m
l_{mc}, m_{mc}, d_{mc}	=	aerodynamic lift, moment, and drag on an airfoil about its midchord
$\mathbf{M}$, $\mathbf{C}$, $\mathbf{K}$	=	discrete mass, damping, and stiffness matrices of whole system
$\mathbf{M}^{\text{dist}}$, $\mathbf{M}^{\text{pt}}$	=	distributed and point moments
$\mathbf{M}_{FF}$, $\mathbf{C}_{FF}$, $\mathbf{K}_{FF}$	=	generalized mass, damping, and stiffness matrices
$\mathbf{N}$	=	influence matrix for the gravity force
$\mathbf{p}_w$	=	position of w frame resolved in B frame
Q	=	total charge accumulated over the electrodes, C
R	=	resistance of energy harvesting circuit, Ω
$\mathbf{R}_F$	=	components of the generalized load vector
s	=	beam curvilinear coordinate, m
s_p	=	spanwise length of the piezoelectric layer, m
t_p	=	thickness of the piezoelectric layer, m
U_∞	=	aircraft trim velocity or freestream velocity, m/s
v	=	voltage of energy harvesting system, V
W^{ext}, W^{int}	=	external and internal virtual work
w	=	local beam frame resolved in B frame
$\dot{y}$, $\dot{z}$	=	airfoil translational velocity components resolved in local aerodynamic frame, m/s
z_p	=	distance between the elastic axis of the beam and the piezoelectric layer, m
$\dot{\alpha}$	=	airfoil angular velocity about a_{0x} axis, rad/s
$\boldsymbol{\varepsilon}$	=	total beam strain vector
$\bar{\boldsymbol{\varepsilon}}$	=	material strain in piezoelectric constitutive relation
$\boldsymbol{\varepsilon}_0$	=	initial beam strain vector
ε_x	=	extensional strain beam members
$\boldsymbol{\zeta}$	=	permittivity, F/m
$\boldsymbol{\theta}$	=	rotations of beam nodes, rad
κ_x, κ_y, κ_z	=	torsional, flat bending, and in-plane bending curvatures of beam members, 1/m
$\boldsymbol{\lambda}$	=	inflow states, m/s
λ_0	=	inflow velocities, m/s

Presented as Paper 2015-0444 at the 56th AIAA/ASCE/AHS/ASC Structures, Structural Dynamics, and Materials Conference, Kissimmee, FL, 5–9 January 2015; received 12 April 2015; revision received 25 August 2015; accepted for publication 7 September 2015; published online 22 February 2016.

*Ph.D. Student, Department of Aerospace Engineering and Mechanics; ntsushima@crimson.ua.edu. Student Member AIAA.

†Assistant Professor, Department of Aerospace Engineering and Mechanics; suw@eng.ua.edu. Senior Member AIAA.

ρ = air density, kg/m^3
$\bar{\sigma}$ = material stress in piezoelectric constitutive relation, Pa
σ_w = gust intensity, m/s
Φ = power spectrum density function, m^2/s
ω = frequency components of gust signal, rad/s

Subscript

$h\varepsilon$ = $\mathbf{h}$ vector with respect to the strain $\boldsymbol{\varepsilon}$
$p\varepsilon$ = nodal position $\mathbf{p}_w$ with respect to the strain $\boldsymbol{\varepsilon}$
$\theta\varepsilon$ = nodal rotation $\boldsymbol{\theta}$ with respect to the strain $\boldsymbol{\varepsilon}$

I. Introduction

FOR several years, unmanned aerial vehicles (UAVs) have been developed for different applications. For example, the U.S. Air Force has been working on a new generation of intelligence, surveillance, and reconnaissance (ISR) platform, called Sensorcraft [1]. NASA initiated the Environmental Research Aircraft and Sensor Technology program, aimed at developing UAVs capable of very high-altitude and long-endurance flights for atmospheric research proposes. Under this program, an evolutionary series of unmanned aircraft (Pathfinder, Pathfinder-Plus, Centurion, and Helios Prototype) were developed by AeroVironment, Inc. [2]. These high-altitude long-endurance (HALE) UAVs feature slender wings with a high aspect ratio and a low structural mass. Because of the nature of being slender, such wings may undergo large deformations under their normal operation conditions, resulting in geometrically nonlinear behaviors [3–9], such as nonlinear deformations, limit-cycle oscillations, etc. Therefore, geometrical nonlinearity must be taken into account in the aeroelastic modeling of these vehicles. Different nonlinear aeroelastic tools have been developed for accurate prediction of the behavior of HALE vehicles. Without being complete, some relevant examples in this area can be found in Refs. [5,6,10–18], and readers may refer to the references for further information.

At the same time, new structural technologies are under development, which may bring revolutionary changes to aircraft structures [19–23]. Among these new technologies, multifunctional structures are capable of performing multiple primary functions and can potentially improve aircraft performance through consolidation of subsystem materials and functions [24–30]. The combination of new structural technologies and aeroelastic design and analysis methods may synergize to create new highly flexible UAV designs, which may enhance the effectiveness and improve the capability of such aircraft by consolidating the structural weight without sacrificing the aeroelastic and flight performance requirements.

Among the new developments of UAVs, there is growing interest in designing energy-saving autonomous UAV systems. Onboard energy harvesting is considered as a significant approach to design such autonomous systems and push the flight envelop while reducing the weight [27,31–36]. This results in self-sustained multifunctional wing structures that include subsystems of sensing, energy harvesting, energy storage, and actuating. The mechanical vibrations of structural components due to in-flight gust perturbations and limit-cycle oscillations caused by aeroelastic instabilities are potentially a major energy source. With piezoelectric materials (e.g., QuickPack® QP10n) embedded in wing structures as sensors and harvesters, elastic strain energy may be converted to electric charge. On the other hand, piezoelectric actuation can induce the desired mechanical deformation through applied electric potential [33] for active vibration control of the autonomous system.

To explore a potential approach of enhancing the flight performance of highly flexible autonomous aircraft, this paper will focus on the modeling of energy harvesting using piezoelectric materials for such aircraft. In previous studies [36,37], piezoelectric vibration-based energy harvesting has been considered as a possible solution because of the potential to supply additional power without a significant weight penalty. Anton and Inman [32] investigated the possibility of harvesting vibration and solar energy by performing flight experiments in which a UAV's wing spar with surface-mounted piezoelectric patches was able to generate a power of 11.3 μW in the level flight, which was useful for low-power sensor systems. Thus, piezoelectric energy harvesting is attractive because it may reduce the total weight of an aircraft by providing power supplies to its sensing and actuating systems, eliminating the electrical and hydraulic lines.

Many research groups from different fields have developed approaches to model the electromechanical behavior of piezoelectric energy harvesters. Early studies have modeled the piezoelectric energy harvester using a simplified lumped model with beam-bending vibrations [35,38]. Even though the approach was effective, the lumped model had some disadvantages, such as the over simplification of the real physics. To improve the accuracy, some distributed models have been applied in the subsequent studies. For example, Bilgen et al. [39] modeled the cantilever beam with embedded piezoelectric materials using the linear Euler–Bernoulli beam theory. This approach has been applied to the energy harvesting and gust alleviation of a small UAV [31]. Sodano et al. [40] developed a model of the piezoelectric power-harvesting device based on works of Hagood et al. [41] and Crawley and Anderson [42]. They used energy methods to develop the constitutive equations of a bimorph piezoelectric cantilever beam. The model was solved with the Rayleigh–Ritz procedure. Erturk and Inman [43] provided corrections and necessary clarifications for physical assumptions in energy harvesting. More recently, De Marqui et al. [34] presented an electromechanically coupled finite-element plate model for predicting the electrical power output of piezoelectric energy harvester plates. Anton et al. [44] presented the investigation of a multifunctional energy harvesting and energy-storage wing spar for UAVs.

However, most of the preceding works were based on linear beam theories, which cannot capture the nonlinear behavior of highly flexible multifunctional wings. To accurately predict the dynamic behavior of such slender multifunctional wings with energy harvesting (and active control in the future studies), the aeroelastic model should (1) be effective in modeling nonlinear aeroelasticity and flight dynamics of highly flexible aircraft, (2) consider the coupling with electromechanical effects of the piezoelectric materials (both energy harvester and actuator), and (3) facilitate the control design of energy harvesting and actuation. As a requirement, the modeling should be based on a geometrically nonlinear aeroelastic solution of highly flexible vehicles. The strain-based aeroelastic formulation [6–8] has been applied in the studies on different highly flexible configurations. The beam formulation makes no approximation to the deformation of the beam reference line, which is geometrically exact and can accurately model the large deformations of composite beams. Moreover, it solves directly for the beam curvatures that are the variables measured by typical sensors in control studies (e.g., strain gauges). In this study, the geometrically nonlinear aeroelastic formulation [6–8] will be coupled with the electromechanical equations for piezoelectric materials. This is the accurate approach to integrally model energy harvesting and active control of highly flexible aircraft with piezoelectric materials. In addition, simulations of the slender multifunctional wings under gust perturbations, as a source of the piezoelectric energy harvesting, will be performed in the time domain using stochastic gust histories, instead of applying the gust power spectrum density functions in the frequency domain. Such time-domain gust and energy harvesting analysis will capture the real nonlinear behaviors of aircraft in free flight, which is difficult to obtain from frequency–domain analyses.

To summarize, the theoretical formulation of piezoelectric energy harvesting will be presented first in this paper. The multifunctional modeling is based on a strain-based geometrically nonlinear aeroelastic formulation, allowing for the energy harvesting from large deformations of slender wings. The developed multifunctional wing model will then be validated against the experimental vibration tests from Sodano et al. [40], followed by some numerical studies on the piezoelectric energy harvesting of a highly flexible multifunctional wing from its nonlinear vibrations caused by the aeroelastic instability or external wind gusts, where passive vibration suppression will also be discussed with some tuned piezoelectric parameters. From this work, a transient analysis tool is created for energy harvesting simulations of highly flexible multifunctional wings, considering the geometrically nonlinear effects.

II. Theoretical Formulation

The theoretical formulation involved in this study is introduced in this section, where piezoelectric energy harvesters are modeled in a strain-based beam formulation. The strain-based beam [45] and aeroelastic [7,8] formulations have been introduced in the literature. In the beam formulation, the structural members are allowed fully coupled three-dimensional bending, twisting, and extensional deformations. Finite-state inflow theory [46] is incorporated for aerodynamic loads on lifting surfaces.

A. Multifunctional Wing Structure

Figure 1 illustrates a multifunctional beam with both energy harvesting and actuation capabilities, using piezoelectric materials. The current work will only focus on the modeling of the energy harvesting. For simplicity, the harvester converts the energy of beam oscillations in the out-of-plane (flat) bending direction to the electric energy.

The constitutive equation for piezoelectric materials is given as

$$\begin{Bmatrix} \bar{\boldsymbol{\sigma}} \\ \bar{\boldsymbol{B}} \end{Bmatrix} = \begin{bmatrix} \boldsymbol{D} & -\boldsymbol{e}^T \\ \boldsymbol{e} & \boldsymbol{\zeta} \end{bmatrix} \begin{Bmatrix} \bar{\boldsymbol{\varepsilon}} \\ \boldsymbol{E} \end{Bmatrix} \tag{1}$$

in which $\bar{\boldsymbol{\sigma}}$ is the material stress, $\bar{\boldsymbol{B}}$ is the electric displacement, $\mathbf{D}$ is the piezoelectric material stiffness matrix, $\mathbf{e}$ is the piezoelectric coupling, $\boldsymbol{\zeta}$ is the permittivity, $\bar{\boldsymbol{\varepsilon}}$ is the material strain, and $\mathbf{E}$ is the electric field, which is obtained from the gradient of the electric voltage v across the piezoelectric layer:

$$\boldsymbol{E} = \begin{Bmatrix} E_x \\ E_y \\ E_z \end{Bmatrix} = \begin{Bmatrix} -v_{,x} \\ -v_{,y} \\ -v_{,z} \end{Bmatrix} \tag{2}$$

The coupled electromechanical effect of piezoelectric material will be considered when deriving the equations of motion.

B. Fundamental Descriptions of Beam Model

A cantilever beam will be defined in a fixed frame B. A local beam frame (w) is built within the B frame (see Fig. 2), which is used to define the position and orientation of each node along the beam reference line. Vectors $\mathbf{w}_x(s,t)$, $\mathbf{w}_y(s,t)$, and $\mathbf{w}_z(s,t)$ are bases of the beam frame w, the directions of which are pointing along the beam reference axis, toward the leading edge, and normal to the beam (wing) surface, respectively, resolved in the B frame. The curvilinear beam coordinate s provides the nodal location within the body frame.

To model the elastic deformation of slender beams, a nonlinear beam element is developed in the work of [45,47]. Each of the elements has three nodes and four local strain degrees of freedom, which are extension, twist, out-of-plane bending curvature (κ_y), and in-plane bending curvature (κ_z), respectively, of the beam reference line:

$$\boldsymbol{\varepsilon}^T(s) = \{\, \varepsilon_x(s) \quad \kappa_x(s) \quad \kappa_y(s) \quad \kappa_z(s) \,\} \tag{3}$$

which is not to be confused with the strain of the materials ($\bar{\boldsymbol{\varepsilon}}$) in Eq. (1), even though they are related.

Positions and orientations of each node along the beam are determined by a vector consisting of 12 components, which is denoted as

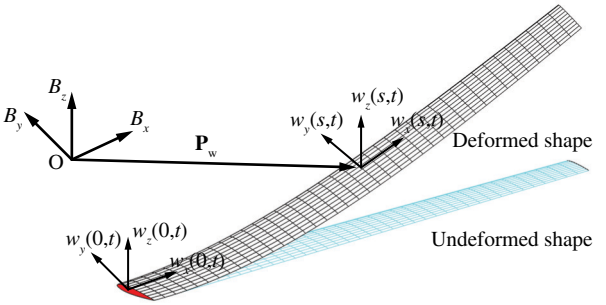

Fig. 2 Beam references frames.

$$\boldsymbol{h}^T(s) = \{\, \boldsymbol{p}_w^T(s) \quad \boldsymbol{w}_x^T(s) \quad \boldsymbol{w}_y^T(s) \quad \boldsymbol{w}_z^T(s) \,\}^T \tag{4}$$

in which $\mathbf{p}_w$ is the nodal position resolved in the B frame and the orientation is represented by the base vectors of the w frame ($\mathbf{w}_x$, $\mathbf{w}_y$, and $\mathbf{w}_z$). The derivative and variation-dependent variable $\mathbf{h}$ are derived from those of the independent variable $\boldsymbol{\varepsilon}$ using the Jacobians, given as

$$\delta\boldsymbol{h} = \boldsymbol{J}_{h\varepsilon}\delta\boldsymbol{\varepsilon} \quad d\boldsymbol{h} = \boldsymbol{J}_{h\varepsilon}d\boldsymbol{\varepsilon} \quad \dot{\boldsymbol{h}} = \boldsymbol{J}_{h\varepsilon}\dot{\boldsymbol{\varepsilon}} \quad \dot{\boldsymbol{h}} = \boldsymbol{J}_{h\varepsilon}\dot{\boldsymbol{\varepsilon}} + \dot{\boldsymbol{J}}_{h\varepsilon}\dot{\boldsymbol{\varepsilon}} \tag{5}$$

in which the Jacobians are obtained from kinematics [12,45]

$$\boldsymbol{J}_{h\varepsilon} = \frac{\partial \boldsymbol{h}}{\partial \boldsymbol{\varepsilon}} \qquad \boldsymbol{J}_{p\varepsilon} = \frac{\partial \boldsymbol{p}_w}{\partial \boldsymbol{\varepsilon}} \qquad \boldsymbol{J}_{\theta\varepsilon} = \frac{\partial \boldsymbol{\theta}}{\partial \boldsymbol{\varepsilon}} \tag{6}$$

with $\mathbf{J}_p\boldsymbol{\varepsilon}$ and $\mathbf{J}_\theta\boldsymbol{\varepsilon}$ being additional Jacobians relating the nodal position and orientation to the elemental strain [12,45].

C. Equations of Motion

The equations of motion are derived by following the principle of virtual work. A detailed derivation in which the electromechanical coupling effect was not considered is found in Su and Cesnik [7,45]. In the new development, the internal virtual work will include contributions of inertia forces, internal strains, and strain rates, as well as those of the electromechanical effects. The internal virtual work of the multifunctional beam is given as

$$\begin{aligned} \delta W^{\text{int}} = {} & -\delta\boldsymbol{h}^T\boldsymbol{M}\ddot{\boldsymbol{h}} - \delta\boldsymbol{\varepsilon}^T\boldsymbol{C}\dot{\boldsymbol{\varepsilon}} - \delta\boldsymbol{\varepsilon}^T\boldsymbol{K}(\boldsymbol{\varepsilon} - \boldsymbol{\varepsilon}_0) + \delta\boldsymbol{\varepsilon}^T\boldsymbol{B}_v v \\ & + \delta v\left(\boldsymbol{B}_v^T\boldsymbol{\varepsilon} + \zeta\frac{b_p s_p}{t_p}v\right) \end{aligned} \tag{7}$$

in which $\boldsymbol{\varepsilon}_0$ is the initial strain of the beam and $\mathbf{B}_v$ is the electromechanical coupling matrix, obtained from the cross-sectional value:

$$\begin{aligned} \boldsymbol{B}_v &= [0 \quad 0 \quad B_v \quad 0]^T \\ B_v &= B_v^{cs}s_p = s_p\int_A -\frac{z_p e_{31}}{t_p}\,\mathrm{d}A \end{aligned} \tag{8}$$

in which A is the cross-section area of the piezoelectric layer. z_p is the distance between the elastic axis of the beam and the piezoelectric layer (see Fig. 3). Quantities b_p, t_p, and s_p are the width, thickness, and length of the piezoelectric layer, respectively. The capacitance of the energy harvester is defined as

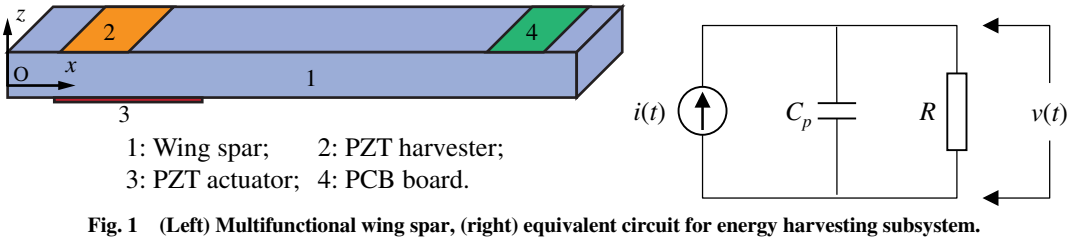

Fig. 1 (Left) Multifunctional wing spar, (right) equivalent circuit for energy harvesting subsystem.

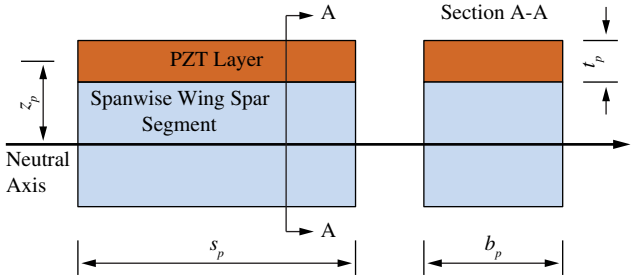

Fig. 3 Spanwise segment and cross section of multifunctional wing spar.

$$C_p = \zeta_{31}\frac{b_p s_p}{t_p} \tag{9}$$

Note that when the bimorph structure connecting piezoelectric layers in parallel is considered, the electromechanical coupling and capacitance will be doubled. The external work includes contributions of gravitational force, distributed force, distributed moment, point force, point moment, and the work of the electric charge of the piezoelectric layer. The total external virtual work is

$$\delta W^{\text{ext}} = \delta \boldsymbol{h}^T \boldsymbol{N}\boldsymbol{g} + \delta \boldsymbol{p}_w^T \boldsymbol{B}^F \boldsymbol{F}^{\text{dist}} + \delta\boldsymbol{\theta}^T \boldsymbol{B}^M \boldsymbol{M}^{\text{dist}} + \delta \boldsymbol{p}_w^T \boldsymbol{F}^{\text{pt}} + \delta\boldsymbol{\theta}^T \boldsymbol{M}^{\text{pt}} + \delta v Q \tag{10}$$

in which $\mathbf{g}$, $\mathbf{F}^{\text{dist}}$, $\mathbf{M}^{\text{dist}}$, $\mathbf{F}^{\text{pt}}$, and $\mathbf{M}^{\text{pt}}$ are the gravity field, distributed forces, distributed moments, point forces, and point moments, respectively. $\mathbf{N}$, $\mathbf{B}^F$, and $\mathbf{B}^M$ are the influence matrices for the gravitational force, distributed forces, and distributed moments, which come from the numerical integration. In addition, Q is the total charge accumulated over the electrodes, the time derivative of which is the current:

$$\frac{dQ}{dt} = i = \frac{v}{R} \tag{11}$$

Based on Eqs. (7) and (10), the variations of the dependent variables ($\mathbf{h}$, $\mathbf{p}_w$, and $\boldsymbol{\theta}$) and their time derivatives can be replaced by the independent variable ($\boldsymbol{\varepsilon}$) by applying the Jacobians [see Eq. (5)] and their subsets. Therefore, the total virtual work on a beam can be written as

$$\begin{aligned}\delta W = &-\delta\boldsymbol{\varepsilon}^T(\boldsymbol{J}_{h\varepsilon}^T\boldsymbol{M}\boldsymbol{J}_{h\varepsilon}\ddot{\boldsymbol{\varepsilon}} + \boldsymbol{J}_{h\varepsilon}^T\boldsymbol{M}\dot{\boldsymbol{J}}_{h\varepsilon}\dot{\boldsymbol{\varepsilon}} + \boldsymbol{C}\dot{\varepsilon} + \boldsymbol{K}\boldsymbol{\varepsilon} - \boldsymbol{K}\boldsymbol{\varepsilon}_0 - \boldsymbol{B}_v v)\\ &+\delta\boldsymbol{\varepsilon}^T(\boldsymbol{J}_{h\varepsilon}^T\boldsymbol{N}\boldsymbol{g} + \boldsymbol{J}_{p\varepsilon}^T\boldsymbol{B}^F\boldsymbol{F}^{\text{dist}} + \boldsymbol{J}_{\theta\varepsilon}^T\boldsymbol{B}^M\boldsymbol{M}^{\text{dist}} + \boldsymbol{J}_{p\varepsilon}^T\boldsymbol{F}^{\text{pt}} + \boldsymbol{J}_{\theta\varepsilon}^T\boldsymbol{M}^{\text{pt}})\\ &+\delta v(\boldsymbol{B}_v^T\boldsymbol{\varepsilon} + C_p v + Q)\end{aligned} \tag{12}$$

Finally, the variations of the strain and the voltage are both arbitrary, which yields the electromechanical system's equations of motion:

$$\begin{aligned}&\boldsymbol{M}_{FF}\ddot{\boldsymbol{\varepsilon}} + \boldsymbol{C}_{FF}\dot{\boldsymbol{\varepsilon}} + \boldsymbol{K}_{FF}\boldsymbol{\varepsilon} = \boldsymbol{R}_F\\ &\boldsymbol{B}_v^T\boldsymbol{\varepsilon} + C_p v + Q = 0 \quad \text{or} \quad \boldsymbol{B}_v^T\dot{\boldsymbol{\varepsilon}} + C_p\dot{v} + \frac{v}{R} = 0\end{aligned} \tag{13}$$

in which the generalized inertia, damping, stiffness matrices, and generalized force vector are

$$\begin{aligned}&\boldsymbol{M}_{FF}(\boldsymbol{\varepsilon}) = \boldsymbol{J}_{h\varepsilon}^T\boldsymbol{M}\boldsymbol{J}_{h\varepsilon} \qquad \boldsymbol{C}_{FF}(\boldsymbol{\varepsilon},\dot{\boldsymbol{\varepsilon}},\boldsymbol{\beta}) = \boldsymbol{C} + \boldsymbol{J}_{h\varepsilon}^T\boldsymbol{M}\dot{\boldsymbol{J}}_{h\varepsilon} \qquad \boldsymbol{K}_{FF} = \boldsymbol{K}\\ &\boldsymbol{R}_F = \boldsymbol{K}_{FF}\boldsymbol{\varepsilon}_0 + \boldsymbol{J}_{h\varepsilon}^T\boldsymbol{N}\boldsymbol{g} + \boldsymbol{J}_{p\varepsilon}^T\boldsymbol{B}^F F^{\text{dist}} + \boldsymbol{J}_{\theta\varepsilon}^T\boldsymbol{B}^M\boldsymbol{M}^{\text{dist}}\\ &\quad + \boldsymbol{J}_{p\varepsilon}^T\boldsymbol{F}^{\text{pt}} + \boldsymbol{J}_{\theta\varepsilon}^T\boldsymbol{M}^{\text{pt}} + \boldsymbol{B}_v v\end{aligned} \tag{14}$$

As shown in Eq. (14), the generalized force vector involves the effects from initial strains $\boldsymbol{\varepsilon}_0$, gravitational field $\mathbf{g}$, distributed forces $\mathbf{F}^{\text{dist}}$, distributed moments $\mathbf{M}^{\text{dist}}$, point forces $\mathbf{F}^{\text{pt}}$, point moments $\mathbf{M}^{\text{pt}}$, and the electric field v. The aerodynamic forces and moments are considered as distributed loads.

D. Unsteady Aerodynamics

The distributed loads, $\mathbf{F}^{\text{dist}}$ and $\mathbf{M}^{\text{dist}}$ in Eq. (14) are divided into aerodynamic loads and user-supplied loads. The unsteady aerodynamic loads used in the current study are based on the two-dimensional (2-D) finite-state inflow theory, provided in Peters and Johnson [46]. The theory calculates aerodynamic loads on a thin airfoil section undergoing large motions in an incompressible inviscid subsonic flow. The lift, moment, and drag of a thin 2-D airfoil section about its midchord are given by

$$\begin{aligned}l_{\text{mc}} &= \pi\rho b_c^2(-\ddot{z} + \dot{y}\dot{\alpha} - d\ddot{\alpha}) + 2\pi\rho b_c\dot{y}^2\left[-\frac{\dot{z}}{\dot{y}} + \left(\frac{1}{2}b_c - d\right)\frac{\dot{\alpha}}{\dot{y}} - \frac{\lambda_0}{\dot{y}}\right]\\ m_{\text{mc}} &= 2\pi\rho b_c^2\left(-\frac{1}{2}\dot{y}\dot{z} - \frac{1}{2}d\dot{y}\dot{\alpha} - \frac{1}{2}\dot{y}\lambda_0 - \frac{1}{16}b_c^2\ddot{\alpha}\right)\\ d_{\text{mc}} &= -2\pi\rho b_c\left(\dot{z}^2 + d^2\dot{\alpha}^2 + \lambda_0^2 + 2d\dot{\alpha}\dot{z} + 2d\dot{\alpha}\lambda_0\right)\end{aligned} \tag{15}$$

in which b_c is the semichord and d is the distance of the midchord in front of the reference axis. The quantity $-\dot{z}/\dot{y}$ is the angle of attack that consists of the contribution from both the steady state angle of attack and the unsteady plunging motion of the airfoil. The different velocity components are shown in Fig. 4. The inflow velocity λ_0 accounts for induced flow due to free vorticity, which is the weighted summation of the inflow states λ as described by Peters and Johnson [46] and governed by

$$\dot{\boldsymbol{\lambda}} = \boldsymbol{F}_1\ddot{\boldsymbol{\varepsilon}} + \boldsymbol{F}_2\dot{\boldsymbol{\varepsilon}} + \boldsymbol{F}_3\boldsymbol{\lambda} \tag{16}$$

The aerodynamic loads about the midchord center are transferred to the wing elastic axis and rotated into the fixed B frame for the solution of equations of motion.

E. Gust Modeling

The Dryden and von Karman [48] gust models are the classical approaches to describe the atmosphere turbulence using the power spectral density (PSD) functions. Because the Dryden PSD function has a simpler form than that of the von Karman model, which facilitates the generation of gust signals, it is chosen in the current studies, although the von Karman gust model can be applied in future works because it agrees better with experimental data [49]. The PSD function is given as

$$\Phi_w(\omega) = \frac{\sigma_w^2 L_w\left[1 + 3\left(\frac{L_w\omega}{U_\infty}\right)^2\right]}{\pi U_0\left[1 + 3\left(\frac{L_w\omega}{U_\infty}\right)^2\right]^2} \tag{17}$$

in which σ_w is the root mean square (RMS) vertical gust velocity, L_w is the scale of turbulence, and U_∞ is the aircraft trim velocity. The scale length L_w is dependent on the aircraft's altitude H, given as

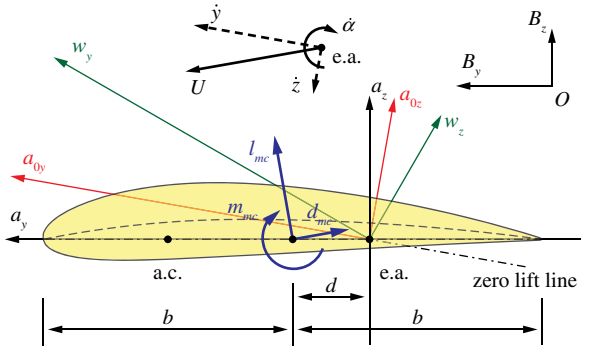

Fig. 4 Airfoil coordinate system and velocity components (a.c., aerodynamic center; mc, midchord; e.a., elastic axis).

Table 1 Properties of the QuickPack QP40N

Property	Symbol	Value
Device size, mm	—	$100.6 \times 25.4 \times 0.762$
Device weight, g	—	9.52
Piezoelectric wafer size, mm	—	$45.974 \times 20.574 \times 0.254$
Relative permittivity	ζ_{33}/ζ_0	1800
Piezoelectric strain coefficient, pm/V	d_{13}	−179
Modulus of piezoelectric, GPa	c_E	63
Modulus of Kapton-epoxy, GPa	c_s	2.5
Modulus of QuickPack, GPa	c_b	35.17
Density of piezoelectric material, kg/m^3	ρ_p	7700
Density of composite matrix, kg/m^3	ρ_c	2150

$$L_w = \begin{cases} 533.4 & H \geq 609.6 \text{ m} \\ \frac{228.6}{304.8}(H + 101.6) & 304.8 \leq H < 609.6 \text{ m} \\ H & H < 304.8 \text{ m} \end{cases} \tag{18}$$

Note that the value between 304.8 and 609.6 m is obtained by the linear interpolation. The gust intensity is determined by

$$\sigma_w = 0.1 w_{20}, \qquad w_{20} = \begin{cases} 7.72 \text{ m/s (weak)} \\ 15.43 \text{ m/s (moderate)} \\ 23.15 \text{ m/s (strong)} \end{cases} \tag{19}$$

in which w_{20} is the wind speed at 20 ft (6 m) height altitude. Typically, for weak turbulence, the wind speed at 6 m is 7.72 m/s; for moderate turbulence, the wind speed is 15.43 m/s; and for strong turbulence, the wind speed is 23.15 m/s. For a very strong turbulence, the wind speed is chosen as 75 m/s, over three times higher than that of the strong turbulence.

Gust signals will be generated using the inputs of the gust intensity, scale length, and PSD function at a given flight velocity and altitude. In doing so, a Gaussian white noise source with the PSD function $\Phi_n(\omega) = 1$ in the frequency band of interest is used to provide the input signal to a linear filter (transfer function) $H_w(s)$, which is chosen such that the squared magnitude of its frequency response is the PSD function $\Phi_w(\omega)$. The output from the transfer function is then the random continuous gust, the PSD of which is related to the PSD of the input signal as follows:

$$\Phi_w(\omega) = |H_w(\omega)|^2 \Phi_n(\omega) = |H_w(\omega)|^2 \tag{20}$$

Finally, an expression for the Dryden model's transfer function can be found through spectral factorization of $\Phi_w(\omega)$, which is

$$H_w(s) = \sigma_w \sqrt{\frac{L_w}{\pi U_\infty}} \frac{1 + \sqrt{3} L_w / U_\infty \, s}{(1 + L_w / U_\infty \, s)^2} \tag{21}$$

III. Numerical Validation

The theoretical formulation is firstly applied to simulate a slender beam with an attached Midé Technology Corporation QuickPack model QP40N and compared to the vibration tests performed in Ref. [40]. The properties of QP40N are shown in Table 1 [40], where the permittivity of free space ζ_0 is 8.854 pF/m. In the experiment, QuickPack QP40N was clamped at the point of 92.6 mm from the free end and mounted to an electromagnetic shaker. As a validation, some experimental cases in Ref. [40] are numerically reproduced using the developed formulation.

Figure 5 compares the numerical and experimental output currents from the harvester when shaken at 25 Hz with two different resistors. Note that due to the high-frequency response in the experiment, only the contours of the experimental data, showing the magnitudes of the vibrational data, are measured and plotted in the figure for the comparison with the numerical data. The output currents across the 10 and 100 kΩ resistors, respectively, with the 50 Hz excitation are shown in Fig. 6. From the figures, the peak values from the simulation fall in a 6% difference from the measured experimental data. Even though the frequencies of the current outputs from the numerical simulations are not directly compared to the experiments, because accurate frequency data are not available based on the plots in Ref. [40], it is still reasonable to conclude that the predictions of the electric outputs by the numerical model with different beam vibrations and resistive loads are accurate.

To verify the convergence of the finite-element discretization of the piezoelectric properties, the reverse (actuation) effect of the piezoelectric material is studied with the same QuickPack QP40N device. A constant external voltage (5 V) is applied across the QP40N, resulting in the static beam flat bending deformation. Even though the beam mesh is refined, the beam tip vertical deflections remain the same (see Fig. 7). From Eq. (8), mesh refinement changes the discrete piezoelectric coupling matrix B_v proportionally to the elemental stiffness matrix. Therefore, the resulting flat bending curvature (κ_y) is the same, no matter how the mesh is refined. Even though the static beam deformation is insensitive to the refinement of the mesh, a ten-element mesh is then used to discretize the beam, while the externally applied voltage is varying. The beam flat bending curvature (κ_y) is proportional to the applied voltage according to Eq. (13). The tip deflection, however, is determined by the nonlinear kinematical relation [12,45], which is not proportional to the applied voltage due to the geometrical nonlinear effect (see Fig. 8).

Prediction of energy harvesting from the beam vibration may be sensitive to the mesh. In this case, a sinusoidal force of 1 N magnitude and 10 Hz frequency is applied at the wing tip in the vertical direction. Figure 9 shows the instantaneous tip vertical deflection and the total voltage output from the beam at the end of two cycles (0.2 s) with the change of the number of beam elements. Both the deflection and the voltage output converge within a 1% relative error, when the beam is discretized into nine elements.

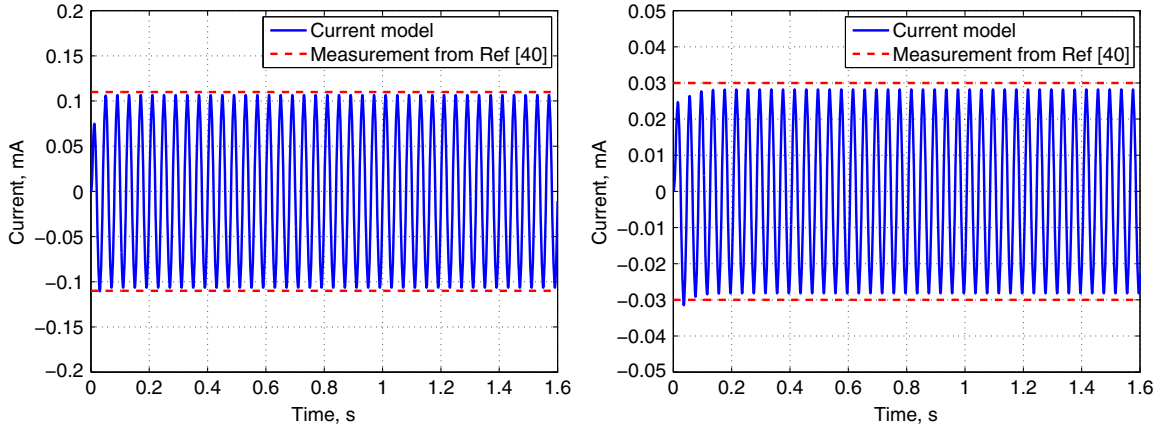

Fig. 5 Output current with 10 kΩ (left) and 100 kΩ (right) resistors with 25 Hz excitation.

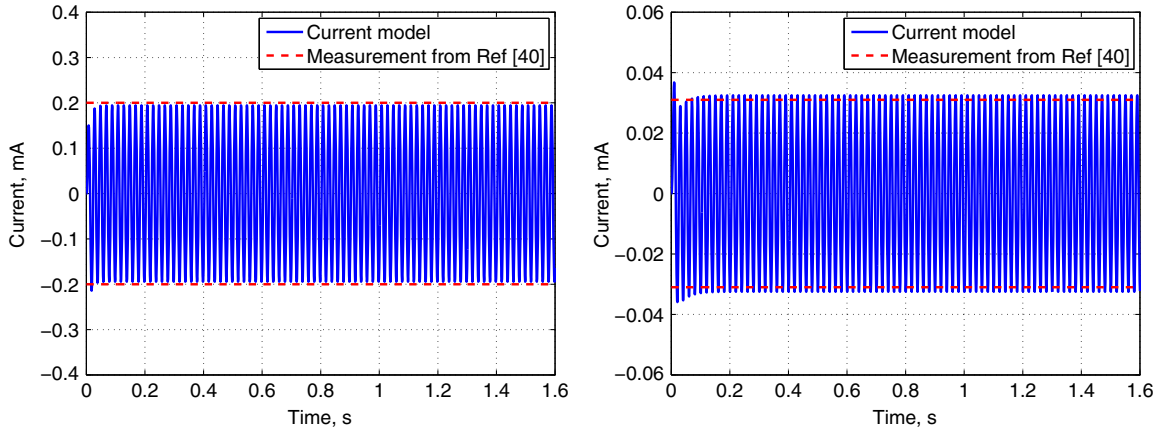

Fig. 6 Output current with 10 kΩ (left) and 100 kΩ (right) resistors with 50 Hz excitation.

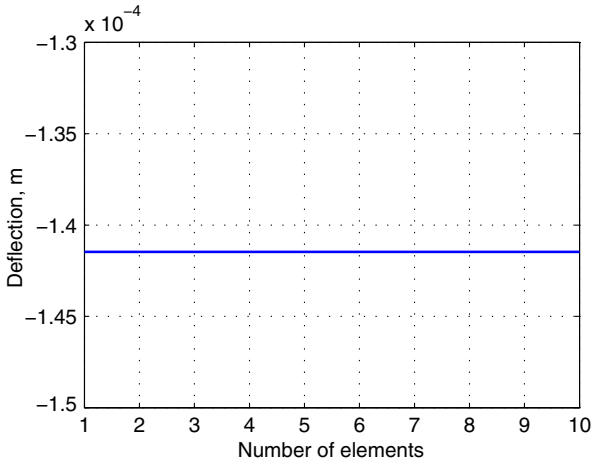

Fig. 7 Static beam tip deflection due to applied 5 V voltage, with mesh refinement.

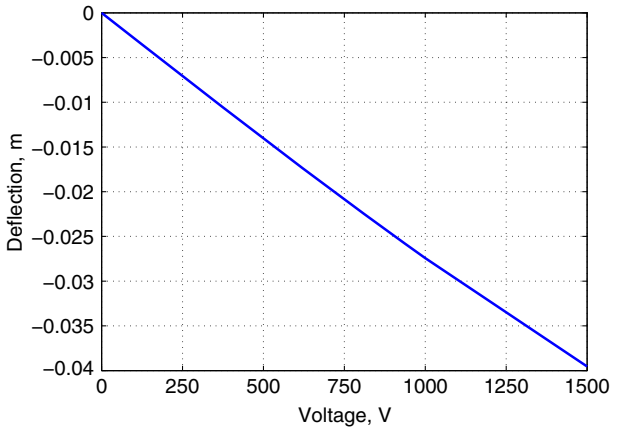

Fig. 8 Static beam tip deflection due to variable applied voltages.

IV. Numerical Studies

In this section, energy harvesting from the transient vibrations of a slender wing, using the derived electroaeroelastic formulation, is presented. Limit-cycle oscillations and wing vibrations excited by wind gusts are considered as the sources of the energy harvesting. In addition, shunt damping effects are studied for passive vibration suppression.

A. Highly Flexible Cantilever Wing for Energy Harvesting

As a piezoelectric energy harvesting system, a highly flexible cantilever wing is designed with a PZT-5A thin film attached to the

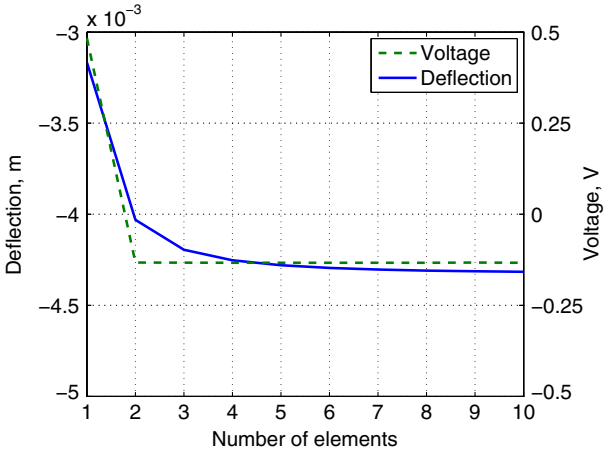

Fig. 9 Instantaneous beam tip deflection and voltage output at the end of two excitation cycles with varying beam mesh.

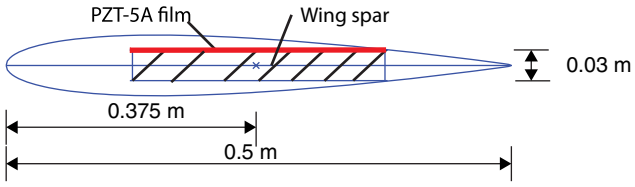

Fig. 10 Cross section of the wing model.

wing spar (see Fig. 10). The wing airfoil is NACA0012. The wing spar has a thickness of 0.03 m and a width of 0.25 m, located at 0.375 m from the leading edge. The physical and geometrical properties of the wing and PZT-5A film are given in Table 2, and more of the piezoelectric properties of PZT-5A can be found in Ref. [33].

Table 2 Properties of the multifunctional wing

Property	Value
Mass per unit length, m	0.09375
Extensional stiffness, K_{11}, N	4.34×10^6
Torsional stiffness, K_{22}, N · m^2	2.71×10^3
Out-of-plane bend stiffness, K_{33}, N · m^2	5.43×10^3
In-plane bend stiffness, K_{44}, N · m^2	1.09×10^6
Torsional moment of inertia, I_{xx}, kg · m	0.0035
Out-of-plane bend moment of inertia, I_{yy}, kg · m	0.0189
In-plane bend moment of inertia, I_{zz}, kg · m	0.0221
Span, m	8
Chord length, m	0.5
PZT-5A width, m	0.25
PZT-5A thickness, m	2.54×10^{-4}
Transverse piezoelectric coupling e_{31}, C/m^2	−10.4

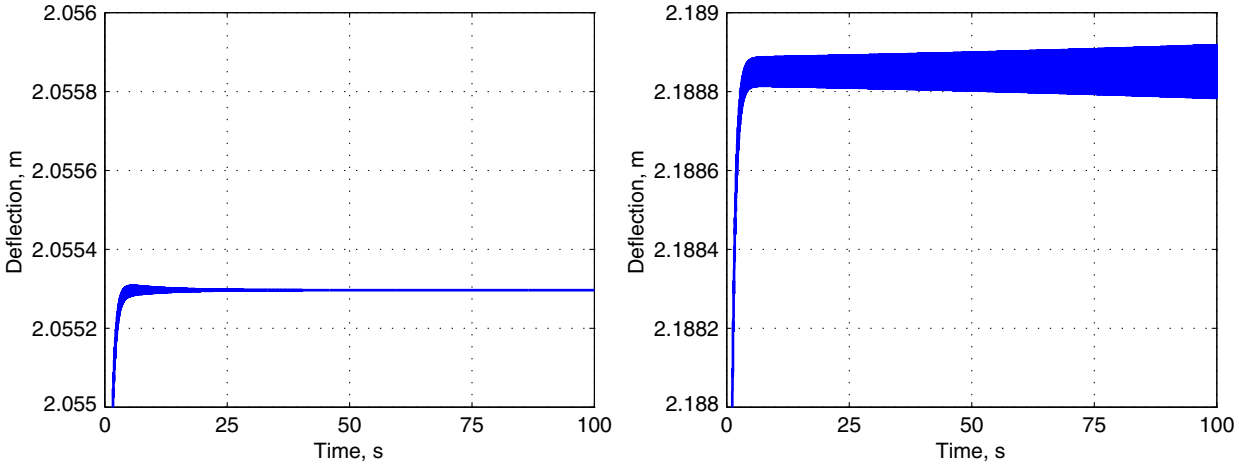

Fig. 11 Wing vertical tip deflection at preflutter ($U_\infty = 51$ m/s, left) and postflutter ($U_\infty = 52$ m/s, right) conditions.

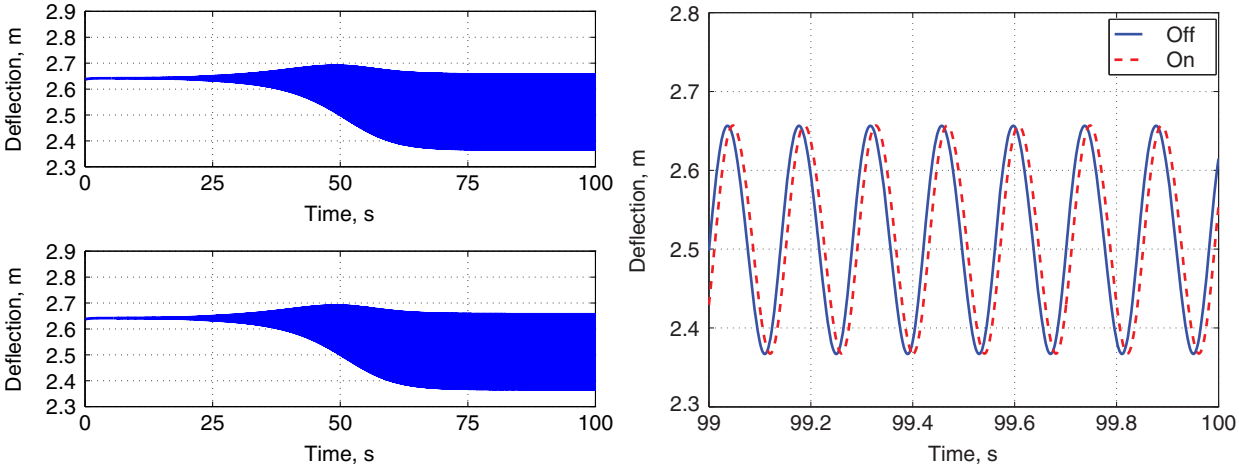

Fig. 12 Tip deflection at $U_\infty = 55$ m/s without (top left) and with (bottom left) energy harvesting function, with the close-up plot for time range of 99 to 100 s (right).

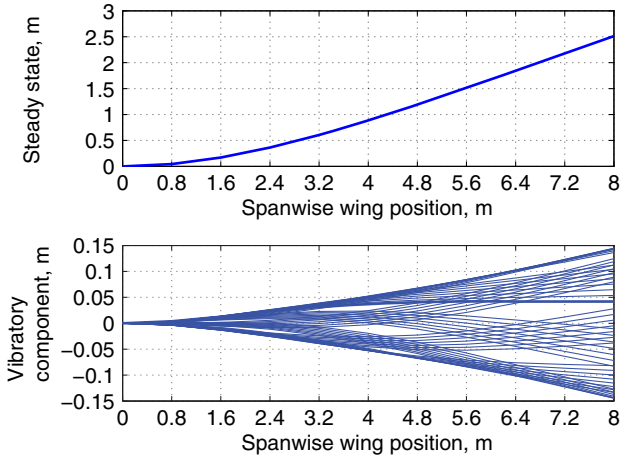

Fig. 13 Wing steady-state deformation and snapshots of vibratory component between 90 and 100 s.

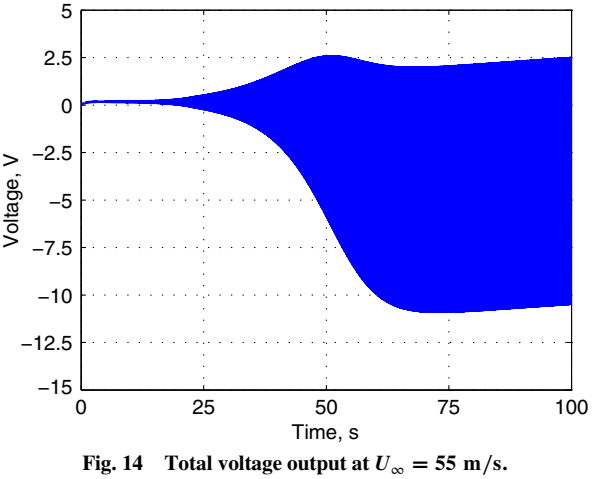

Fig. 14 Total voltage output at $U_\infty = 55$ m/s.

Table 3 Root mean square voltage output (V_{rms}, V) on each harvesting element with different piezoelectric couplings

	Element ID (from root)									
Piezoelectric coupling (e_{31}, C/m^2)	1	2	3	4	5	6	7	8	9	10
–10.4	1.743	1.142	0.911	0.960	1.009	0.938	0.748	0.487	0.225	0.045
–416	0.094	0.328	0.541	0.624	0.573	0.394	0.129	0.168	0.417	0.616

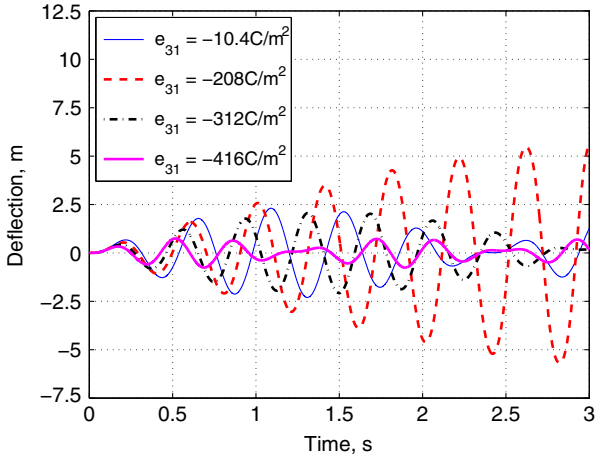

Fig. 15 Tip deflection of the wing with various electric coupling (resistance $R = 1$ MΩ).

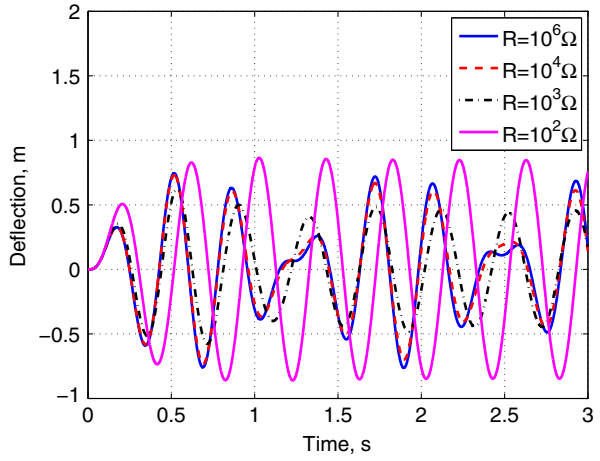

Fig. 16 Tip deflection of the wing with various resistances (piezoelectric coupling $e_{31} = -416$ C/m^2).

The wing cross-sectional properties are unified based on the properties of both the spar and the PZT-5A film. The wing is divided into 10 elements. Each element is modeled as an independent energy harvester. To complete the circuit, a resistance of 1 MΩ is used.

B. Energy Harvesting from Aeroelastic Instability

From time-domain simulations, the flutter instability of the highly flexible wing can be observed when the freestream velocity U_∞ is about 52 m/s, as shown in Fig. 11. Note that in these simulations, the energy harvesting function is still turned off, even though the piezoelectric materials are already embedded in the wing structure. If the freestream velocity is slightly above the flutter boundary, the growth of vibration amplitude will be very slow due to the small aeroelastic damping. Therefore, the following studies will be performed at a higher freestream velocity $U_\infty = 55$ m/s to facilitate the observation of the limit-cycle oscillations. Figure 12 shows the limit-cycle oscillations with the energy harvesting function turned off and on, at the 55 m/s freestream velocity. Because a one-layered PZT harvester is used in this case, no significant piezoelectric shunt damping effect can be observed. Even though the behaviors look very close to each other, a slight phase change can be seen in this case from Fig. 12 (right), which shows the results between 99 and 100 s of the two simulations. The phase change indicates the impact of the energy harvester subsystem on the system behavior as an additional load component to the aeroelastic system [see Eq. (14)]. According to the snapshots of the wing deformations between 90 and 100 s (see Fig. 13), both the first and second out-of-plane bending vibration modes can be observed in addition to the steady-state deformation of the beam. Correlating with such a deformation mode, both the root and middle portions of the wing may provide higher voltage outputs, where the local strains are relatively larger than the rest locations along the wing, as can be observed from the RMS voltage (V_{rms}) outputs from each harvester or element (see Table 3, line of $e_{31} = -10.4$ C/m^2). Figure 14 illustrates the total voltage output from the energy harvesting system. With this wing configuration attached with a single-layered PZT5-A film, the total RMS voltage output from the postflutter limit-cycle oscillation between 90 and 100 s is 5.78 VAC, which will be adequate for powering onboard low-power sensors (e.g., temperature sensors) of the airplane.

The piezoelectric shunt damping of the multifunctional wing is then tuned to study the impact of the passive shunt damping effect [50] on the wing vibration. A parametric study is performed here without using a sophisticated optimization scheme. In this study, a sinusoidal distributed force with a 5 N/m magnitude and a 2.5 Hz frequency is applied along the vertical direction of the wing. The vertical wing tip deflections are observed with the change of the piezoelectric properties. It can be noticed that this study only tunes the shunt damping with a structural vibration, without considering the fluid–structure interaction. However, the tuned piezoelectric parameters will be further applied to the aeroelastic energy harvesting and passive vibration control study in the following section, as long as the limit-cycle oscillation can be effectively suppressed by using the tuned parameters. For the study here, the piezoelectric effect is magnified by increasing the piezoelectric coupling term e, which is almost equivalent to increasing the number of PZT5-A film layers, resulting in a multilayered piezoelectric film. However, the structural properties are assumed to be unchanged even with the use of the multilayered PZT5-A film. Figure 15 shows the result, where a large reduction of the vibration magnitude is observed, with the piezoelectric coupling e_{31} being -416 C/m^2. Note that the increase of

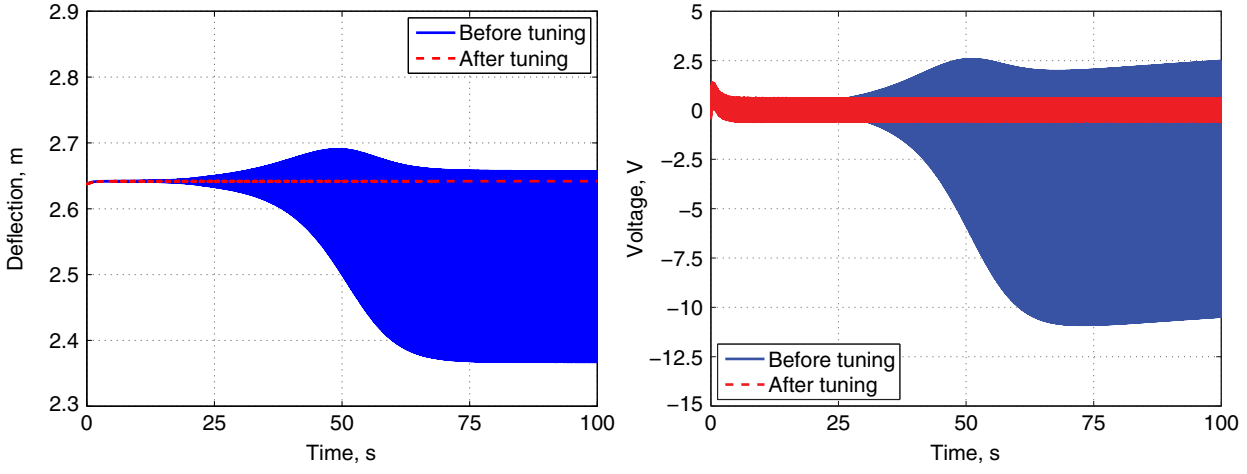

Fig. 17 Tip deflection and total voltage output at $U_\infty = 55$ m/s with tuned parameters.

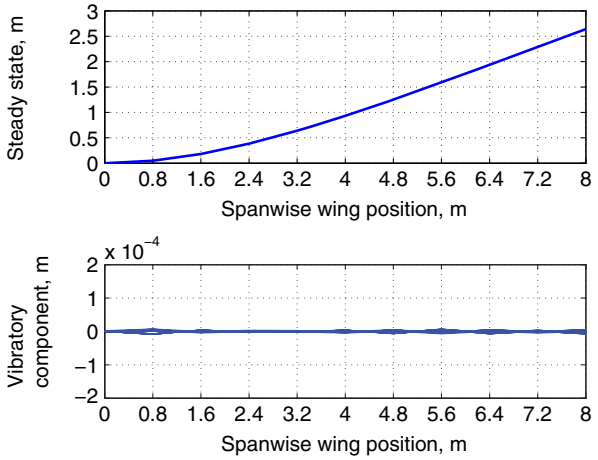

Fig. 18 Steady-state deformation and snapshots of vibratory component of the tuned wing between 90 and 100 s.

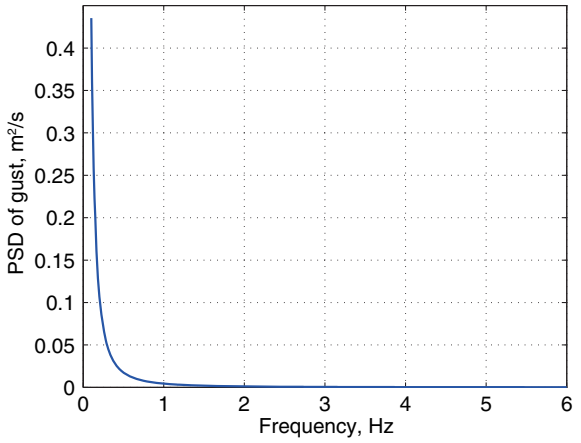

Fig. 19 PSD function of strong ($\sigma_w = 2.315$ m/s) gust turbulences at $h = 20{,}000$ m.

piezoelectric coupling constant e_{31} is equivalent to the increase of piezoelectric layers without geometrical change. There exists a specific value of the piezoelectric coupling constant (around -208 C/m^2 in this case) at which the resonant shunt gets mistuned and loses its damping, resulting in the increased vibration magnitude. On the other hand, the resistance load is changed down to 100 Ω while keeping the piezoelectric coupling e_{31} as -416 C/m^2. The results are shown in Fig. 16. The system with 1 kΩ resistance shows an overall reduction in the vibration magnitude.

The investigation on the fluttering multifunctional wing is further performed. In this case, the piezoelectric coupling e_{31} is tuned to be -416 C/m^2, and resistance R is changed to 1 kΩ. Even though the freestream velocity is still above the flutter boundary, the wing vibration is suppressed by the single-mode shunt damping effect (see Fig. 17), which can be clearly observed from the comparison with the baseline case. A low-voltage output is still available, as long as the vibration is not completely damped out. The output voltage from each element is listed in Table 3 (line of $e_{31} = -416$ C/m^2). Figure 18 shows the steady-state deformation and snapshots of the vibratory component of the tuned wing between 90 and 100 s. Compared with the deformation shown in Fig. 13, the vibration of the

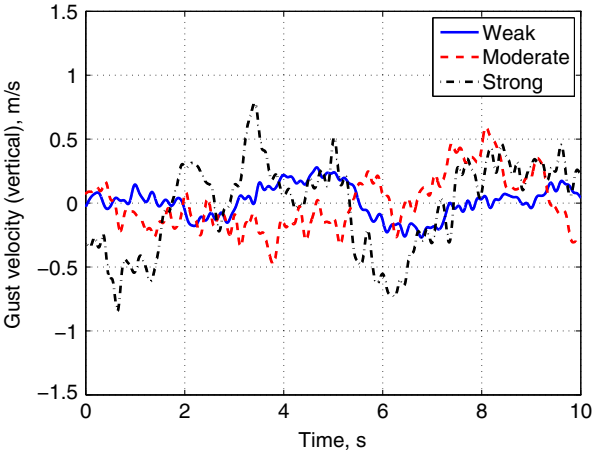

Fig. 20 Gust time histories of weak ($\sigma_w = 0.772$ m/s), moderate ($\sigma_w = 0.772$ m/s), and strong ($\sigma_w = 2.315$ m/s) turbulences at $h = 20{,}000$ m.

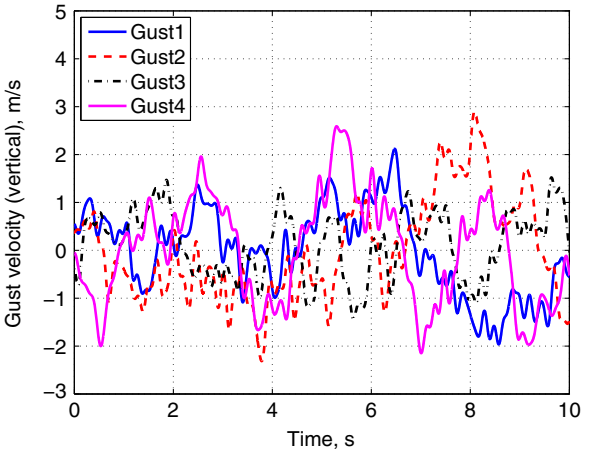

Fig. 21 Gust time history of very strong ($\sigma_w = 7.5$ m/s) turbulence at $h = 20{,}000$ m.

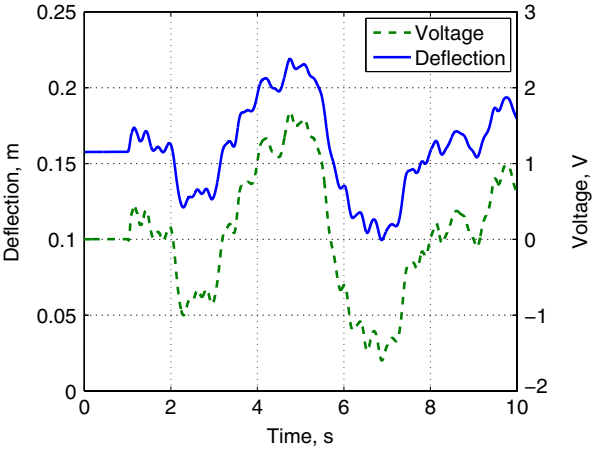

Fig. 22 Tip deflection and total voltage output with weak turbulence at $h = 20{,}000$ m, $U_\infty = 18$ m/s.

Table 4 Gust signals and output voltage

	Typical turbulence			Very strong turbulence			
Category	Weak	Moderate	Strong	Gust1	Gust2	Gust3	Gust4
Gust intensity, m/s	0.77	1.54	2.32	7.50	7.50	7.50	7.50
Frequency band, Hz	0.1–6.0	0.1–6.0	0.1–6.0	0.1–6.0	0.1–6.0	0.1–6.0	0.1–6.0
Output V_{rms}, V	0.81	1.34	2.01	5.61	6.53	4.00	6.68

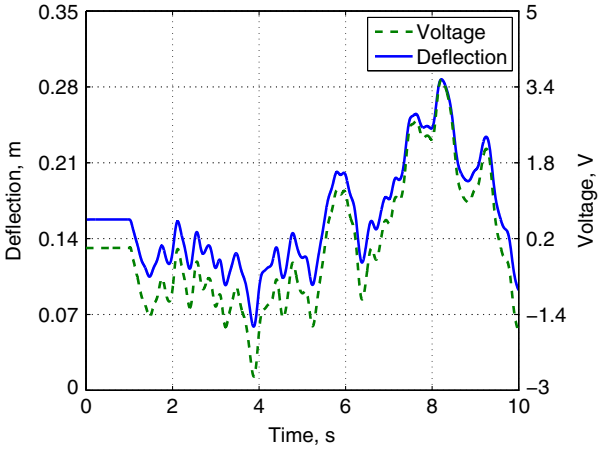

Fig. 23 Tip deflection and total voltage output with moderate turbulence at $h = 20{,}000$ m, $U_\infty = 18$ m/s.

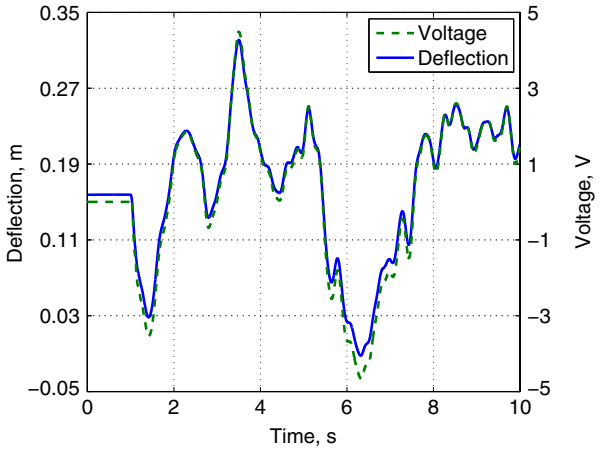

Fig. 24 Tip deflection and total voltage output with strong turbulence at $h = 20{,}000$ m, $U_\infty = 18$ m/s.

tuned wing is almost, but not completely, suppressed by the shunt damping. Because of the shut damping, the dominant vibration mode is changed, resulting in the change of curvature as well as the voltage output on each element. The total output voltage amplitude at the end of 100 s is about 0.58 VAC, and the total RMS voltage output from the postflutter limit-cycle oscillation between 90 and 100 s is 0.36 VAC.

From this study, the capability of harvesting electric energy from the mechanical wing vibrations has been demonstrated. Passive vibration suppression by a tuned piezoelectric harvesting device is also verified to be feasible. Further exploration can be made to tune the shunt damping while balancing between the vibration suppression and the necessary vibration for the energy harvesting. The optimal multifunctional material placement will also need to be considered.

C. Energy Harvesting from Gust Excitations

Energy harvesting of the highly flexible wing with the one-layered harvester under gust perturbations are investigated using the developed model. The flight altitude is 20,000 m, and the speed is 18 m/s. The Dryden gust model is applied to generate gust signals to represent typical weak, moderate, and strong turbulence, as well as very strong turbulences. Because of the randomness of the gust, four gust time histories are generated for the very strong cases from the same PSD function. When the gust signals are generated, the frequencies of gust components are all truncated at 6 Hz, because the energies of high-frequency gusts are small, as shown in Fig. 19.

The summary of the simulation cases and the corresponding total voltage outputs are tabulated in Table 4. Figures 20 and 21 show the time histories of the gust signals, and the resulting wing tip deflections and voltage outputs from each case are plotted in Figs. 22–25. Note the wing hits the gusts after 1 s into the simulations. The voltage outputs are 0.81, 1.34, and 2.01 V from the weak, moderate, and strong turbulence, respectively. The output can be increased to 5.71 V with the very strong turbulences (an average of the four simulations). Again, this amount would be possible to power up the aforementioned low-power sensors. As can be seen from the results, the wing tip displacements under the very strong turbulences are already large, yet the voltage outputs are not sufficient for regular flight control applications (e.g., gust alleviation). Therefore, more layers of the piezoelectric materials are necessary to allow more energy to be harvested. In addition, it will be more feasible to convert the AC outputs from the energy harvesting to DC signals and accumulate the energy in a storage subsystem for planned flight control applications.

V. Conclusions

An approach for the modeling of energy harvesting from transient vibrations of slender wing structures using piezoelectric transduction was introduced in the paper. A strain-based geometrically nonlinear beam formulation was enhanced with the electromechanical model of the piezoelectric effect. Large deformations, especially the limit-cycle oscillations, of slender multifunctional beams were accurately captured. This can provide an accurate approach to integrally model energy harvesting and active control of highly flexible multifunctional wings with piezoelectric materials. For aeroelastic analysis, finite-state unsteady subsonic aerodynamic loads were coupled to the wing surface. The coupled electroaeroelastic model enabled the prediction of the electric outputs and the mechanical deformations with piezoelectric shunt damping under external wing excitations. The numerical simulations were run in a computer with dual processors at 3.10 GHz and 8 GB memory. All simulations can be finished within 1–8 h,

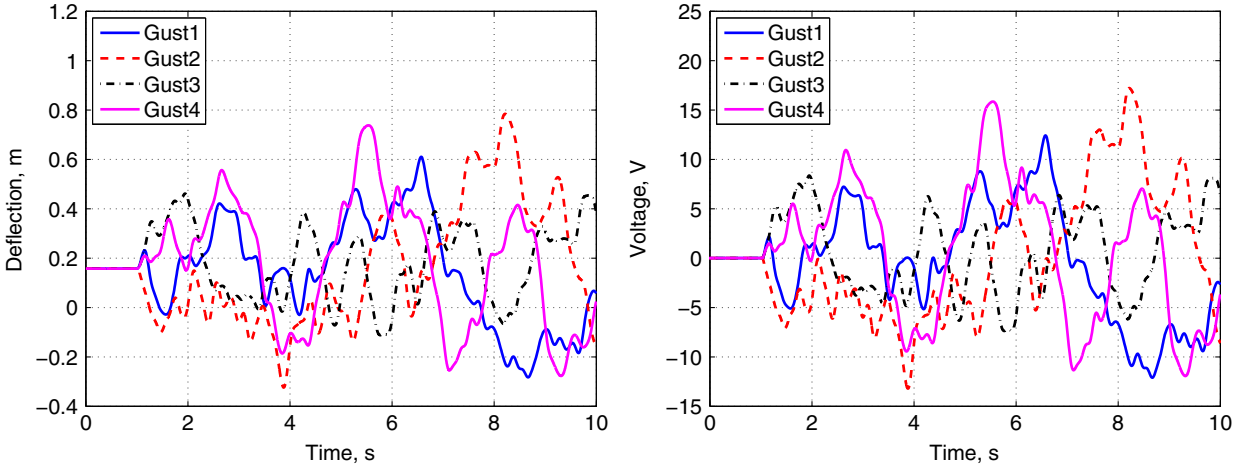

Fig. 25 Tip deflection and total voltage output from very strong turbulences at $h = 20{,}000$ m, $U_\infty = 18$ m/s.

depending on the length of the simulated time duration. Therefore, the numerical multifunctional aeroelastic formulation is considered as efficient, due to the benefit of the low-order formulations.

Based on the validated multifunctional wing model, piezoelectric energy harvesting from the wing vibrations due to the aeroelastic instability and wind gust excitations was studied. Stochastic gust signals created based on the Dryden gust model were applied in time-domain energy harvesting analyses. This allows for accurate estimation of the nonlinear behaviors and energy harvesting of slender multifunctional wings. With the highly flexible cantilever wing designed for the energy harvesting simulations, the flutter boundary was estimated as 52 m/s. Energy harvesting from the transient vibration was simulated at a freestream velocity of 55 m/s. With a single-layered PZT-5A film, the estimated total output voltage was about 6.5 V. Moreover, the piezoelectric shunt damping effect became more prominent with a tuned multilayered piezoelectric harvester. Therefore, with a well-tuned piezoelectric structure, one could potentially either harvest the vibrational energy or suppress the wing vibration. Because the voltage output from the piezoelectric energy harvesting system was dependent on the wing deformation, the shunt damping effects would change the elemental voltage output while impacting the wing vibration behavior. Electric energy can also be harvested from the wing vibrations due to gust perturbations. With the Dryden gust model, typical turbulences of weak, moderate, and strong intensity were studied. They may produce about 1–2 V output with the specific wing configuration. The very strong turbulence provided an average of 5.71 V output from four independent time histories of the gust.

From the study, an efficient system with dual functions of both energy harvesting and passive vibration suppression may be developed by optimizing the piezoelectric shunt damping. The optimization should be performed considering the balance between the vibration reduction and the required harvesting energy amount. Because of the intermittent behavior of gust and the alternating current from the direct harvested energy, an energy regulation and storage subsystem is necessary so as to accumulate the harvested electric energy to support in-flight aircraft control. After all, this study provides a foundation of the integral energy harvesting and active vibration control of highly flexible aircraft with multifunctional structures in free flight. Development of a robust, energy-saving control algorithm to actuate the multifunctional system for vibration control will be part of the future work. Future studies will also be extended to the active gust and stability control of such vehicles with the integrated energy harvesting subsystem.

References

[1] Tilmann, C. P., Flick, P. M., Martin, C. A., and Love, M. H., "High-Altitude Long Endurance Technologies for SensorCraft," *Symposium on Novel and Emerging Vehicle and Vehicle Technology Concepts*, RTO-AVT-099, MP-104-P-26, Brussels, April 2003.

[2] Noll, T. E., Brown, J. M., Perez-Davis, M. E., Ishmael, S. D., Tiffany, G. C., and Gaier, M., "Investigation of the Helios Prototype Aircraft Mishap Volume I Mishap Report," Data available online at, http://www.nasa.gov/pdf/64317main_helios.pdf [retrieved 1 Aug. 2015].

[3] Patil, M. J., Hodges, D. H., and Cesnik, C. E. S., "Nonlinear Aeroelastic Analysis of Complete Aircraft in Subsonic Flow," *Journal of Aircraft*, Vol. 52, No. 6, 2000, pp. 753–760. doi:10.2514/2.2685

[4] Patil, M. J., Hodges, D. H., and Cesnik, C. E. S., "Limit-Cycle Oscillations in High-Aspect-Ratio Wings," *Journal of Fluids and Structures*, Vol. 15, No. 1, 2001, pp. 107–132. doi:10.1006/jfls.2000.0329

[5] Patil, M. J., Hodges, D. H., and Cesnik, C. E. S., "Nonlinear Aeroelasticity and Flight Dynamics of High-Altitude Long-Endurance Aircraft," *Journal of Aircraft*, Vol. 38, No. 1, 2001, pp. 88–94. doi: 10.2514/2.2738

[6] Shearer, C. M., and Cesnik, C. E. S., "Nonlinear Flight Dynamics of Very Flexible Aircraft," *Journal of Aircraft*, Vol. 44, No. 6, 2007, pp. 1528–1545. doi:10.2514/1.27606

[7] Su, W., and Cesnik, C. E. S., "Nonlinear Aeroelasticity of a Very Flexible Blended-Wing-Body Aircraft," *Journal of Aircraft*, Vol. 47, No. 6, 2010, pp. 1539–1553. doi:10.2514/1.47317

[8] Su, W., and Cesnik, C. E. S., "Dynamic Response of Highly Flexible Flying Wings," *AIAA Journal*, Vol. 49, No. 2, 2011, pp. 324–339. doi:10.2514/1.J050496

[9] Tang, D., and Dowell, E. H., "Experimental and Theoretical Study on Aeroelastic Response of High-Aspect-Ratio Wings," *AIAA Journal*, Vol. 39, No. 8, 2001, pp. 1430–1441. doi:10.2514/2.1484

[10] U.S. Army Aviation and Missile Command, *RCAS User's Manual, Version 2.0*, Moffett Field, CA,

[11] Drela, M., "Integrated Simulation Model for Preliminary Aerodynamic, Structural, and Control-Law Design of Aircraft," *Proceedings of the 40th AIAA/ASME/ASCE/AHS/ASC Structures, Structural Dynamics, and Materials Conference and Exhibit*, AIAA Paper 1999-1394, 1999, pp. 1644–1656.

[12] Cesnik, C. E., and Brown, E. L., "Modeling of High Aspect Ratio Active Flexible Wings for Roll Control," *Proceedings of the 43rd AIAA/ASME/ASCE/AHS Structures, Structural Dynamics, and Materials Conferences*, AIAA Paper 2002-1719, 2002.

[13] Cesnik, C. E. S., and Su, W., "Nonlinear Aeroelastic Modeling and Analysis of Fully Flexible Aircraft," *Proceedings of the 46th AIAA/ASME/ASCE/AHS/ASC Structures, Structural Dynamics, and Materials Conference*, AIAA Paper 2005-2169, April 2005.

[14] Patil, M. J., and Hodges, D. H., "Flight Dynamics of Highly Flexible Flying Wings," *Journal of Aircraft*, Vol. 43, No. 6, 2006, pp. 1790–1799. doi: 10.2514/1.17640

[15] Shearer, C. M., and Cesnik, C. E. S., "Trajectory Control for Very Flexible Aircraft," *Journal of Guidance, Control, and Dynamics*, Vol. 31, No. 2, 2008, pp. 340–357. doi: 10.2514/1.29335

[16] Chang, C., Hodges, D. H., and Patil, M. J., "Flight Dynamics of Highly Flexible Aircraft," *Journal of Aircraft*, Vol. 45, No. 2, 2008, pp. 538–545. doi:10.2514/1.30890

[17] Dowell, E. H., Edwards, J., and Strganac, T., "Nonlinear Aeroelasticity," *Journal of Aircraft*, Vol. 40, No. 6, 2003, pp. 857–874. doi:10.2514/2.6876

[18] Wang, Z., Chen, P.-C., Liu, D. D., Mook, D. T., and Patil, M. J., "Time Domain Nonlinear Aeroelastic Analysis for Hale Wings," *Proceedings of the 47th AIAA/ASME/ASCE/AHS/ASC Structures, Structural Dynamics, and Materials Conference*, AIAA Paper 2006-1640, 2006.

[19] Pendleton, E., Flick, P., Paul, D., Voracek, D., Reichenbach, E., and Griffin, K., "The X-53 A Summary of the Active Aeroelastic Wing Flight Research Program," *Proceedings of the 48th AIAA/ASME/ASCE/AHS/ASC Structures, Structural Dynamics, and Materials Conference and Exhibit*, AIAA Paper 2007-1855, 2007.

[20] Voracek, D. F., Pendleton, E., and Reichenbach, E., "The Active Aeroelastic Wing Phase I Flight Research Through January 2003," NASA, Dryden Flight Research Center, Edwards AFB, CA, 2003.

[21] Pendleton, E. W., Bessette, D., Field, P. B., and Miller, G. D., "Active Aeroelastic Wing Flight Research Program: Technical Program and Model Analytical Development," *Journal of Aircraft*, Vol. 52, No. 4, 2000, pp. 554–561. doi:10.2514/2.2654

[22] Pendleton, E., Griffin, K. E., Kehoe, M. W., and Perry, B., "A Flight Research Program for Active Aeroelastic Wing Technology," *Proceedings of the 37th AIAA/ASME/ASCE/AHS/ASC Structures, Structural Dynamics, and Materials Conference and Exhibit*, AIAA Paper 1996-1574, 1996.

[23] Karpel, M., "Design for Active Flutter Suppression and Gust Alleviation Using State-Space Aeroelastic Modeling," *Journal of Aircraft*, Vol. 19, No. 3, 1982, pp. 221–227. doi:10.2514/3.57379

[24] Bent, A. A., "Active Fiber Composite Material Systems for Structural Control Applications," *Proceedings of SPIE 3991, Smart Structures and Materials 2000: Industrial and Commercial Applications of Smart Structures Technologies*, edited by Jacobs, J. H., Bellingham, WA, 1999, pp. 166–177.

[25] Wilkie, W. K., Bryant, R. G., High, J. W., Fox, R. L., Hellbaum, R. F., Jalink, A., Jr., Little, B. D., and Mirick, P. H., "Low-Cost Piezocomposite Actuator for Structural Control Applications," *Proceeding of SPIE 3991, Smart Structures and Materials 2000: Industrial and Commercial Applications of Smart Structures Technologies*, edited by Jacobs, J. H., SPIE, Bellingham, WA, 2000, pp. 323–334.

[26] Williams, R. B., Park, G., Inman, D. J., and Wilkie, W. K., "An Overview of Composite Actuators with Piezoceramic Fibers," *Proceeding of 20th*

International Modal Analysis Conference, Los Angeles, 2002, pp. 421–427.

[27] Beeby, S. P., Tudor, M. J., and White, N. M., "Energy Harvesting Vibration Sources for Microsystems Applications," *Measurement Science and Technology*, Vol. 17, No. 12, 2006, pp. R175–R195. doi:10.1088/0957-0233/17/12/r01

[28] Aglietti, G. S., Schwingshackl, C. W., and Roberts, S. C., "Multifunctional Structure Technologies for Satellite Applications," *The Shock and Vibration Digest*, Vol. 39, No. 6, 2007, pp. 381–394. doi:10.1177/0583102407077397

[29] Thomas, J. P., and Qidwai, M. A., "The Design and Application of Multifunctional Structure-Battery Materials Systems," *Journal of the Minerals, Metals and Materials Society*, Vol. 57, No. 3, 2005, pp. 18–24. doi:10.1007/s11837-005-0228-5

[30] Thomas, J. P., Keennon, M. T., DuPasquier, A., and Qidwai, M. A., "Multifunctional Structure-Battery Materials for Enhanced Performance in Small Unmanned Air Vehicles," *ASME 2003 International Mechanical Engineering Congress and Exposition*, American Soc. of Mechanical Engineers IMECE2003-41512, Fairfield, NJ, 2003, pp. 289–292.

[31] Wang, Y., and Inman, D. J., "Simultaneous Energy Harvesting and Gust Alleviation for a Multifunctional Wing Spar Using Reduced Energy Control Laws via Piezoceramics," *Journal of Composite Materials*, Vol. 47, No. 1, 2013, pp. 125–146. doi:10.1177/0021998312448677

[32] Anton, S. R., and Inman, D. J., "Vibration Energy Harvesting for Unmanned Aerial Vehicles," *Proceedings of SPIE 6928, Active and Passive Smart Structures and Integrated Systems 2008*, edited by Ahmadian, M., SPIE, Bellingham, WA, March 2008, Article ID 692824, p. 12.

[33] Erturk, A., and Inman, D. J., "Piezoelectric Energy Harvesting," John Wiley & Sons, Hoboken, NJ, 2011, pp. 1–385.

[34] De Marqui, C., Jr., Erturk, A., and Inman, D. J., "An Electromechanical Finite Element Model for Piezoelectric Energy Harvester Plates," *Journal of Sound and Vibration*, Vol. 327, No. 1, 2009, pp. 9–25. doi:10.1016/j.jsv.2009.05.015

[35] Dutoit, N. E., Wardle, B. L., and Kim, S. G., "Design Considerations for MEMS-Scale Piezoelectric Mechanical Vibration Energy Harvesters," *Integrated Ferroelectrics*, Vol. 71, No. 1, 2005, pp. 121–160. doi:10.1080/10584580590964574

[36] Anton, S. R., and Sodano, H. A., "A Review of Power Harvesting Using Piezoelectric Materials (2003–2006)," *Smart Materials and Structures*, Vol. 16, No. 3, 2007, pp. R1–R21. doi:10.1088/0964-1726/16/3/R01

[37] Sodano, H. A., Inman, D. J., and Park, G., "A Review of Power Harvesting from Vibration Using Piezoelectric Materials," *The Shock and Vibration Digest*, Vol. 36, No. 3, 2004, pp. 197–205.

[38] Roundy, S., and Wright, P. K., "A Piezoelectric Vibration Based Generator for Wireless Electronics," *Smart Materials and Structures*, Vol. 13, No. 6, 2004, pp. 1131–1142. doi:10.1088/0964-1726/13/5/018

[39] Bilgen, O., Wang, Y., and Inman, D. J., "Electromechanical Comparison of Cantilevered Beams with Multifunctional Piezoceramic Devices," *Mechanical Systems and Signal Processing*, Vol. 27, 2012, pp. 763–777. doi:10.1016/j.ymssp.2011.09.002

[40] Sodano, H. A., Park, G., and Inman, D. J., "Estimation of Electric Charge Output for Piezoelectric Energy Harvesting," *Strain*, Vol. 40, No. 2, 2004, pp. 49–58. doi: 10.1111/j.1475-1305.2004.00120.x

[41] Hagood, N. W., Chung, W. H., and von Flotow, A., "Modelling of Piezoelectric Actuator Dynamics for Active Structural Control," *Journal of Intelligent Material Systems and Structures*, Vol. 1, No. 3, 1990, pp. 327–354. doi: 10.1177/1045389X9000100305

[42] Crawley, E. F., and Anderson, E. H., "Detailed Models of Piezoceramic Actuation of Beams," *Journal of Intelligent Material Systems and Structures*, Vol. 1, No. 1, 1990, pp. 4–25. doi: 10.1177/1045389X9000100102

[43] Erturk, A., and Inman, D. J., "Issues in Mathematical Modeling of Piezoelectric Energy Harvesters," *Smart Materials and Structures*, Vol. 17, No. 6, 2008, pp. 1–14. doi:10.1088/0964-1726/17/6/065016

[44] Anton, S. R., Erturk, A., and Inman, D. J., "Multifunctional Unmanned Aerial Vehicle Wing Spar for Low-Power Generation and Storage," *Journal of Aircraft*, Vol. 49, No. 1, 2012, pp. 292–301. doi: 10.2514/1.C031542

[45] Su, W., and Cesnik, C.E.S., "Strain-Based Geometrically Nonlinear Beam Formulation for Modeling Very Flexible Aircraft," *International Journal of Solids and Structures*, Vol. 48, No. 16, 2011, pp. 2349–2360. doi:10.1016/j.ijsolstr.2011.04.012

[46] Peters, D. A., and Johnson, M. J., "Finite-State Airloads for Deformable Airfoils on Fixed and Rotating Wings," *Proceedings of Symposium on Aeroelasticity and Fluid Structure Interaction Problems, ASME Winter Annual Meeting*, Vol. 44, The American Soc. of Mechanical Engineering, New York, 1994, pp. 1–28.

[47] Cesnik, C. E., and Brown, E. L., "Active Warping Control of a Joined-Wing Airplane Configuration," *Proceedings of the 44th AIAA/ASME/ASCE/AHS/ASC Structures, Structural Dynamics, and Material Conference*, AIAA Paper 2003-1715, April 2003.

[48] McLean, D., "*Automatic Flight Control Systems*, " Englewood Cliffs, Prentice Hall, NJ, Vol. 606, 1990, pp. 128–150.

[49] Hoblit, F. M., "*Gust Loads on Aircraft: Concepts and Applications*, " AIAA Education Series, AIAA, Washington, D.C., 1988.

[50] Moheimani, S. O. R., and Fleming, A.J ., *Piezoelectric Transducers for Vibration Control and Damping*, Springer–Verlag, London, 2006, pp. 73–176.